Supporting Information

S-Doped Ni(OH)$_2$ Nano-Electrocatalyst Confined in Semiconductor Zeolite with Enhanced Oxygen Evolution Activity

Dandan Hu,[†‡] Xiang Wang,[†] Xitong Chen,[‡] Yanxiang Wang,[‡] Anh N. Hong,[‡] Jun Zhong,[§] Xianhui Bu,[ǁ] Pingyun Feng*[‡] and Tao Wu*[†]

[†] *College of Chemistry, Chemical Engineering and Materials Science, Soochow University, Suzhou 215123, China*

[‡] *Department of Chemistry, University of California, Riverside, California 92521, USA*

[§] *Institute of Functional Nano & Soft Materials (FUNSOM), Soochow University, Suzhou 215123, China*

[ǁ] *Department of Chemistry and Biochemistry, California State University, Long Beach, California 90840, USA*

E-mail: wutao@suda.edu.cn;

   pingyun.feng@ucr.edu

Experimental Section

Materials Sulfur (S, >99%, powder), germanium oxide (GeO_2, HP, powder), gallium metal (Ga, AP, bulk), cesium chloride (CsCl, 99%, solid), tris(2-aminoethyl)amine (TAEA, 96%, liquid), cesium fluoride (CsF, 99.9%, solid), sodium fluoride (NaF, 99%, solid), lithium fluoride (LiF, 99.9%, solid), nickel(II) chloride hexahydrate ($NiCl_2 \cdot 6H_2O$, 99%, solid), cesium chloride (CsCl, 99%, solid) were used as received without any further purification.

Synthesis of CSZ and Cs@CSZ The chalcogenide semiconductor zeolite of UCR-20-GaGeS-TAEA (denoted as CSZ here) was synthesized according to literature reported previously.[1] Ga (82.7 mg, 1.19 mmol, bulk), S (222.1 mg, 6.93 mmol, powder), GeO_2 (109.1 mg, 1.02 mmol, powder) and TAEA (2.1719 g, liquid) were mixed in a Teflon-lined autoclave at room temperature with vigorous stirring for about 30 min, and an brown suspension was formed. Then, autoclave was sealed in the vessel and heated at 190 °C for 6 days. When the autoclave was cooled to room temperature, pale yellow crystals were obtained, which were then washed with ethanol (95%) and deionized water for several times. To obtain Cs@CSZ, an ion-exchange procedure was performed. 100 mL CsCl (*aq.*) (1.0 mol/L) was repeated in the same batch of CSZ crystals (500 mg) for twice under 85 °C to completely remove H^+-TAEA in the nanopores of CSZ.

Preparation of pure CSZ-NaF CSZ-NaF was prepared by facile soaking method. The detailed procedure was described as following: 30 mg of CSZ sample was placed in 10 mL of NaF (1 mol/L) solution at 85 °C for 20 h. Then, the plastic bottles were cooled down to room temperature, and bits of yellow samples were obtained. The samples were washed with ethanol (95%) and deionized water for several times to remove redundant Na^+ and F^- ions and the generated product of GeF_4 (white powder).

Preparation of Ni(OH)$_2$ NPs@CSZ-MF (1 M) 30 mg of original crystalline CSZ was immersed in the mixed solution with 10 mL of NaF (1 M) and transition metal salt solution ($NiCl_2$, 1 mol/L, 6 mL) at 85 °C for 20 h. Then, the plastic bottles were cooled to room temperature, and black samples were obtained. The obtained samples were washed with ethanol (95 %) and deionized water for several times to remove redundant M^+/ F^- and transition metal salt as well as the generated product of GeF_4. To investigate the effect of different stripping agent, CsF and LiF were utilized subsequently. And the obtained samples were named as Ni(OH)$_2$ NPs@CSZ-CsF (1 M) and Ni(OH)$_2$ NPs@CSZ-LiF (1 M), respectively. By comparison, Cs^+-exchanged sample (Cs^+@CSZ) was also used to prepare Ni(OH)$_2$ NPs@CSZ-NaF (1 M).

Characterization Powder X-ray diffraction (PXRD) patterns of the as-prepared samples were recorded on diffractometer (D8 PHASER, Bruker, Germany) using Cu-Kα radiation operated at 40 kV and 40 mA. Energy dispersive X-ray spectroscopy (EDS) and scanning electron microscope (SEM) were supported by using a scanning electron microscope (SEM/S-4700). Transmission electron microscopy (TEM) and high-resolution TEM (HRTEM) as well as STEM elemental mapping were performed on a FEI Tecnai G2F20 S-Twin TMP apparatus working at an accelerating voltage of 200 kV. X-ray photoelectron spectroscopy (XPS) was measured by using an Escalab 250Xi with one-anode Al Kα monochromatic X-ray source. N_2 absorption-desorption experiments were operated on a Micromeritics ASAP 2020 HD 808 system at 77 K. X-ray Absorption Near Edge Structure (XANES) and Extended X-ray Absorption Fine Structure (EXAFS) data were collected on beamline 14 W at the Shanghai Synchrotron Radiation

Facility (SSRF), beamline 17C1 at the Taiwan Light Source (TLS) and beamline 44A at the Taiwan Photon Source (TPS).

Preparation of working electrode The prepared samples (5 mg) were fully ground and uniformly mixed with 2 mg acetylene black (AB), and then was placed into the mixed solution of 600 μL ethanol and 40 μL nafion (5% wt). Then, the mixed solution was sonicated strongly for about 1 h to form homogenous ink solution. The ink solution (20 μL) was coated onto the pre-cleaned glassy carbon electrode (diameter: 5 mm, area: 0.19625 cm^2) as work electrode and dried at room temperature for the following electrochmical measurements.

Electrochemical measurements Relevant electrochemical measurements were performed in a typical three-electrode electrochemical system and equipped with computer-controlled electrochemistry station (CHI-650E). In three-electrode system, glassy carbon electrode (GCE) covered by catalysts was uutilized as working electrode, KCl saturated Ag/AgCl electrode and platinum electrode were used as the reference electrode and counter electrode, respectively. Cyclic voltammetry (CV) was performed to active catalysts with scan rate of 1 V/s for 200 cycles after purging high pure O$_2$ for 30 min. The process was repeated until the catalytic activity reaches steady state. Linear sweep voltammetry (LSV) was recorded in the O$_2$-saturated 1 M KOH solution from 0 to 1 V (*vs.* Ag/AgCl) with scan rate of 5 mV/s. The electrochemical active surface area (ECSA) of the catalyst was estimated by measuring double-layer capacitance (C_{dl}) under the potential window of 0.4-0.45 *vs.* Ag/AgCl with various scan rate of 20-120 mV/s. The electrochemical impedance spectroscopy (EIS) measurement were performed using a Solartron 1260 impedance/gain-phase analyzer connected to a Solartron 1287 electrochemistry interface. Zplot 2.6b was used as the control software and ZView 2.6b was used as the analysis software. A typical measurement was made over a frequency range between 0.1 MHz to 0.01 Hz and 50 mV (peak voltage) was applied as AC signals. The long-term stability of the catalyst was conducted by cycling the CV between 0 and 1 V vs. Ag/AgCl for 2000 cycles. All electrochemical measurements were measured without *iR*-correction and performed at room temperature. All the potentials that mentioned in the work were converted to the reversible hydrogen electrode (RHE) according the equation 1:

$$E\ (RHE) = E(Ag/AgCl) + 0.197 + pH \times 0.059 \qquad (1)$$

The overpotential (η_{10}) at 10 mA cm^{-2} was calculated by equation 2:

$$\eta_{10} = E(RHE) - 1.23 \qquad (2)$$

The number of 1.23 means the theoretical decomposition voltage ($O_2 \rightarrow H_2O$).

The Tafel slope was calculated by equation 3:

$$\eta = b\log j + a \qquad (3)$$

☐ η is the corresponding overpotential, j (mA/cm^2) is the current density, and b is Tafel slope.

Turnover Frequency (TOF) Calculation

The TOF value was calculated by the equation 4:

$$TOF = \frac{j \times A}{4 \times F \times m} \qquad (4)$$

where j (mA/cm²) is the current density at an overpotential of 300 mV during LSV measurement, A is the area of the glassy carbon electrode (0.19625 cm²), F is the Faraday constant (96485 C/mol), m is the moles of activate sites on the work electrode, and 4 means a four-electron transfer during the OER process.
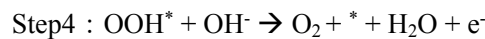
Calculation Method:First-principle calculations were performed by the density functional theory (DFT) using the Vienna Ab-initio Simulation Package (VASP) package[1]. The generalized gradient approximation (GGA) with the Perdew-Burke-Ernzerhof (PBE) functional were used to describe the electronic exchange and correlation effects [2-4]. Uniform G-centered k-points meshes with a resolution of $2\pi*0.03$ Å^{-1} and Methfessel-Paxton electronic smearing were adopted for the integration in the Brillouin zone for geometric optimization. The simulation was run with a cutoff energy of 500 eV throughout the computations. These settings ensure convergence of the total energies to within 1 meV per atom. Structure relaxation proceeded until all forces on atoms were less than 1 meV Å^{-1} and the total stress tensor was within 0.01 GPa of the target value. Due to the strong-correlation of d electrons in Ni, a U−J parameter of 6.45 eV was applied [5].

For the β-Ni(OH)$_2$ systems, the (100) plane was chosen as the reaction surface, since it will predominantly expose Ni atoms in an octahedral environment, and the vacuum space is 12 Å. According to hydrogen electrode (CHE) model, the adsorption free energy for adsorbed species in OER, including OH*, O* and OOH*, can be expressed by the following equation:

$$\Delta G_{ads} = \Delta E_{ads} + \Delta E_{ZPE} - T\Delta S$$

Where ΔE_{ads} is the adsorption energy change of adsorbates, E_{ZPE} is the zero energy calculated from the vibrational frequencies, ΔS is the entropy change, and T is the system temperature (298.15 K, in our work).

Generally, in alkaline media, the OER reaction mechanism can be written as 4-elecetron change mechanism:

$$\text{Step1: } ^* + OH^- \rightarrow OH^* + e^-$$
$$\text{Step2: } OH^* + OH^- \rightarrow O^* + H_2O + e^-$$
$$\text{Step3 : } O^* + OH^- \rightarrow OOH^* + e^-$$
$$\text{Step4 : } OOH^* + OH^- \rightarrow O_2 + ^* + H_2O + e^-$$

where * presents an adsorption site on the catalyst, and OH*, O*, and OOH* denotes the corresponding absorbed intermediates. Accordingly, the free energy of reactions (S1)-(S4) can be calculated using aforementioned equations:

$$\Delta G_1 = G(OH^*) - G(^*) - G(OH^-)$$
$$\Delta G_2 = G(O^*) + G(H_2O) - G(OH^*) - G(OH^-)$$
$$\Delta G_3 = \Delta G(OOH^*) - G(O^*) - G(OH^*)$$
$$\Delta G_4 = 4.92 - \Delta G_1 - \Delta G_2 - \Delta G_3$$

The theoretical overpotential η for OER can be calculated using the equations:

$$G^{OER} = \max \{\Delta G_1, \Delta G_2, \Delta G_3, \Delta G_4\}$$
$$\eta^{OER} = G^{OER}/e - 1.23 \text{ V}$$

Results and Discussion

Comparing the hardness and softness of Ge⁴⁺, Ga³⁺ and Ni²⁺

Based on the hard-soft acid base theory (HSAB), hard base easily combines with hard acid. The hardness and softness of metal ions depended on ionic charge and radius and electronegativity, which can be determined by following equation 5:

$$f = \frac{Z}{r} - 3X + 2.2 \qquad (5)$$

Where Z represents ionic charge, r represent ionic radius, and X represent electronegativity. When f is more than zero, the ion is hard. Conversely, corresponding ions pertain to soft acid/base. $f \cong 0$, the element belongs to border acid/base. By calculating:

$$f_{Ni^{2+}} = \frac{2}{0.69} - 3 \times 1.91 + 2.2 = -0.63$$

$$f_{Ga^{3+}} = \frac{3}{0.61} - 3 \times 1.81 + 2.2 = 1.69$$

$$f_{Ge^{4+}} = \frac{4}{0.53} - 3 \times 2.01 + 2.2 = 3.72$$

$$f_{S^{2-}} = \frac{2}{1.7} - 3 \times 2.58 + 2.2 = -4.36$$

Ge⁴⁺ belongs to the harder acid than Ni²⁺ and Ga³⁺, which suggests that Ge⁴⁺ is more easily bonded with F⁻ (hard base).
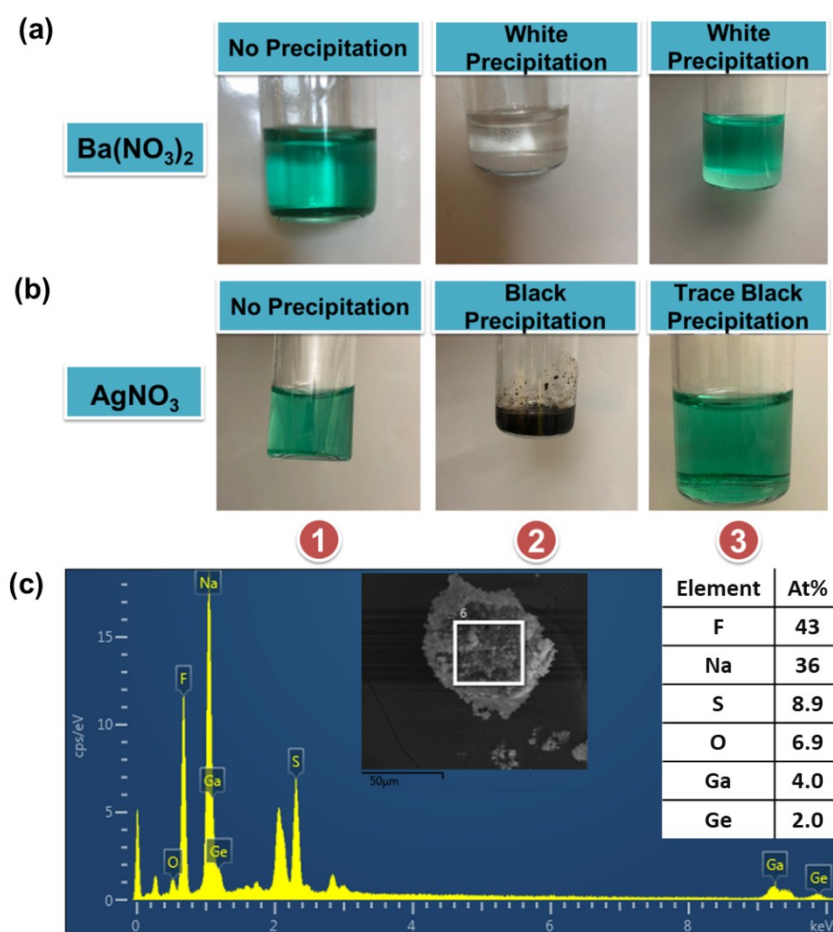
Fig. S1 (a-b) The optical photographs showing exprimental phenonmena when $Ba(NO_3)_2$ (a) and $AgNO_3$ (b) salts were added into specific solutions obtained after centrifugation: (1) NaF *aq.* (10 mL, 1 M) + $NiCl_2$ *aq.* (6 mL, 1 M); (2) CSZ (30 mg) + NaF *aq.* (10 mL, 1 M); (3) CSZ (30 mg) + NaF *aq.* (10 mL, 1 M) + $Ni(NO_3)_2$ *aq.* (6 mL, 1 M). (c) SEM images and the corresponding EDX element analysis of white precipitates from solution 2 after centrifugation.

As shown in **Fig. S1**, no precipitation was observed in solution 1. However, in the mixed solution 2, white precipitation and black precipitation were formed with addition of $Ba(NO_3)_2$ and $AgNO_3$, respectively. This phenomena indicated that SO_4^{2-} and S^{2-} ions existed in the solution. The S^{2-} anions were derived from the etched CSZ when some Ge or Ga ions from CSZ were stripped by F^-. Such S^{2-} anions could be further oxdized by oxygen in air to form SO_4^{2-} ions. There was a similar phenonmenon observed in solution 3 when $Ba(NO_3)_2$ salt was added. To be noticed, only trace of black precipitation was observed when $AgNO_3$ salt was added in solution 3, which indicated that there were small amount of S^{2-} ions in solution. Moreover, some white precipitate can be obtained in solution 2 after centrifugation. And, these precipitates were thought to be the hydrolyzed product of the stripped Ge/Ga species. In order to verity that, EDX element analysis was performed. As shown in **Fig. S1d**, Ga and Ge can be obviously detected, which indicates that partical Ge/Ga ions in CSZ were stripped out of the framewokr by F^-.
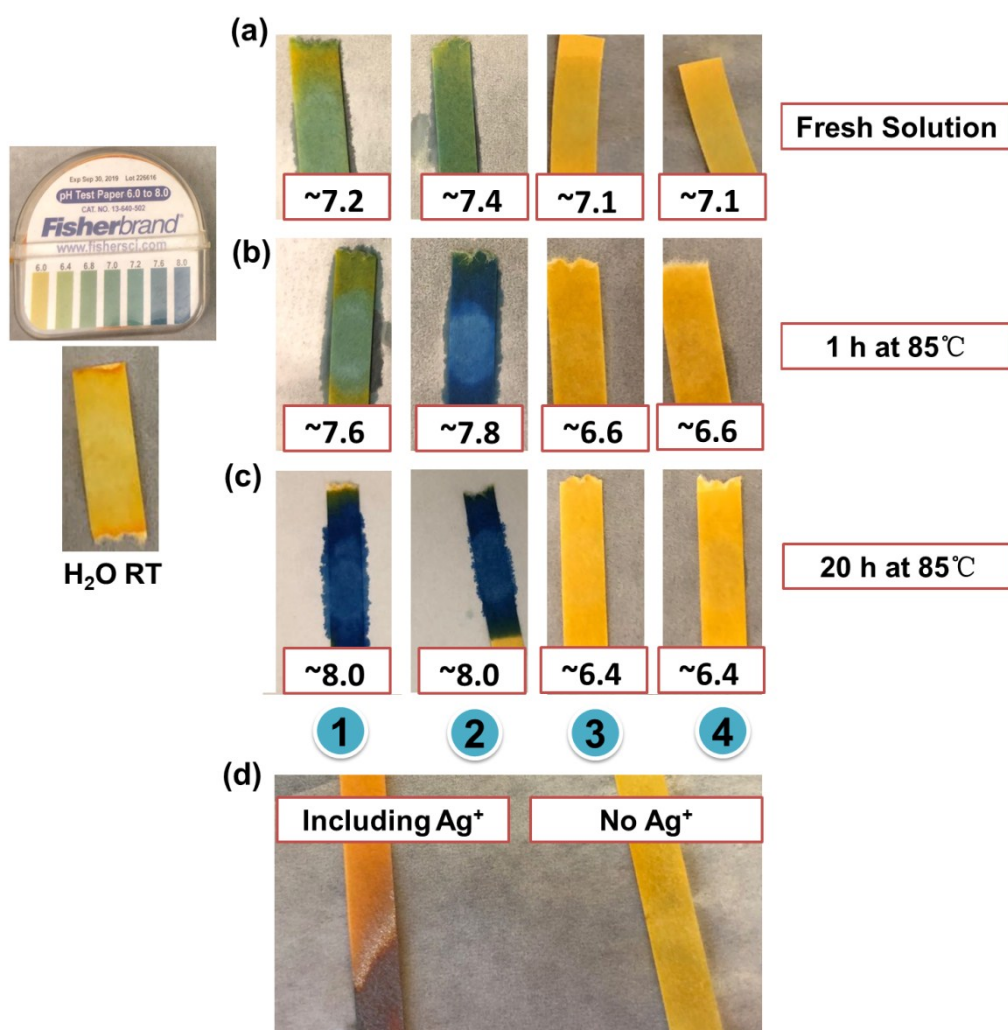
Fig. S2 (a-c) the quantitative detection on pH value of different solutions: (1) pure NaF solution (10 mL, 1 M) + 6 mL water; (2) CSZ (30 mg) + NaF *aq.* (10 mL, 1 M); (3) CSZ (30 mg) + NaF *aq.* (10 mL, 1 M) + $Ni(NO_3)_2$ *aq.* (6 mL, 1 M); (4) CSZ (30 mg) + NaF *aq.* (10 mL, 1 M) + $NiCl_2$ *aq.* (6 mL , 1 M). Notes: (a) fresh solution at RT; (b) 1 h for 85℃; (c) 20 h for 85℃; (d) the detection of H_2S gas in solution 2.

As shown in **Fig. S2**, the pH value of solution 1 gradually increased with the increase of temperture, especially at 85℃, which indicated that the hydrolysis of NaF generated a large amount of OH⁻ ions ($NaF + H_2O \rightarrow NaOH + HF$). And, the solution 2 displayed the similar phenomenon with solution 1. By comparison, the pH value of solution 3 and 4 gradually decreased. Meanwhile, when the caps were opened, the gas with smell of rotten eggs (H_2S) could be detected by nose and test paper. When the test paper include Ag^+, some black precipitate can be observed (**Fig. S2d**).The phenomenon can be explained that the generated OH⁻ was utilized to combine with Ni^{2+} to form $Ni(OH)_2$ nanoparticles, and H^+ ions derived from hydrolysis of NaF reacted with S^{2-} ions from CSZ to form H_2S.
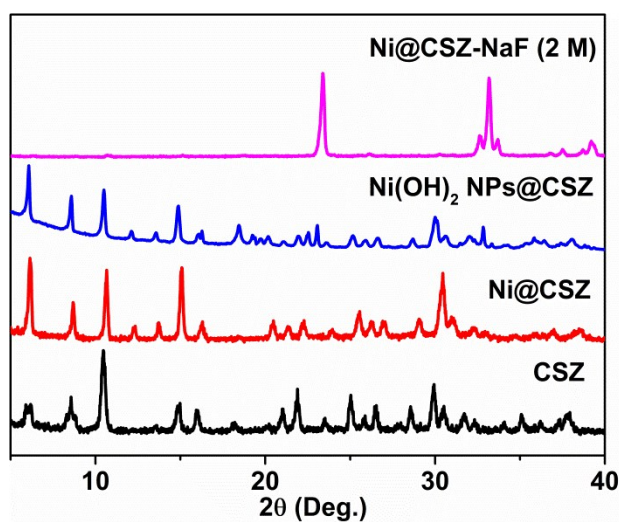
Fig. S3 Powder X-ray diffraction (PXRD) patterns of CSZ, Ni@CSZ, Ni(OH)$_2$ NPs@CSZ and Ni/CSZ-NaF (2 M).
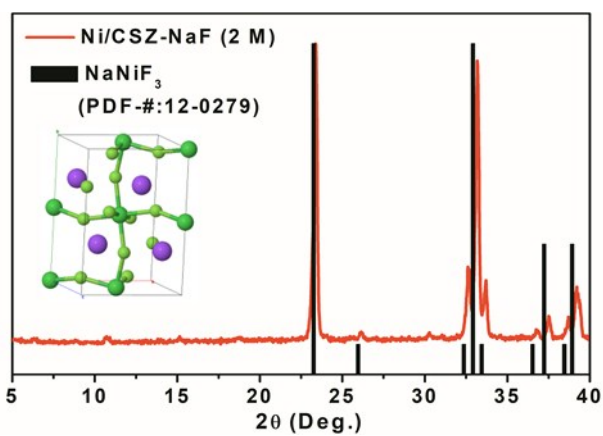
Fig. S4 PXRD patterns of Ni/CSZ-NaF (2 M) and NaNiF$_3$ (**PDF#:12-0279**).
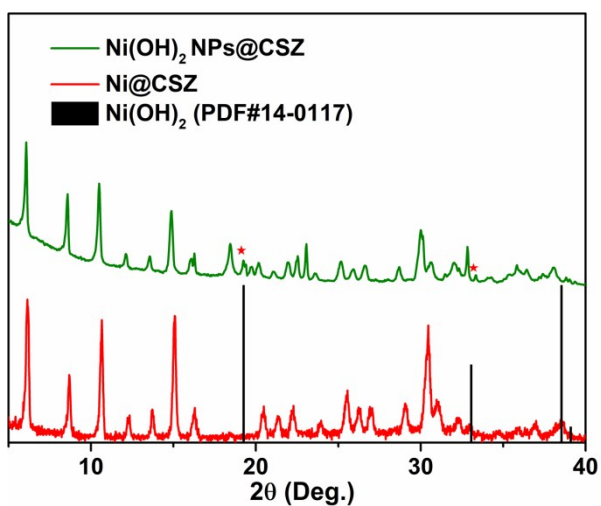

Fig. S5 PXRD patterns of Ni@CSZ, Ni(OH)$_2$ NPs@CSZ and Ni(OH)$_2$ (**PDF-#:14-0117**).
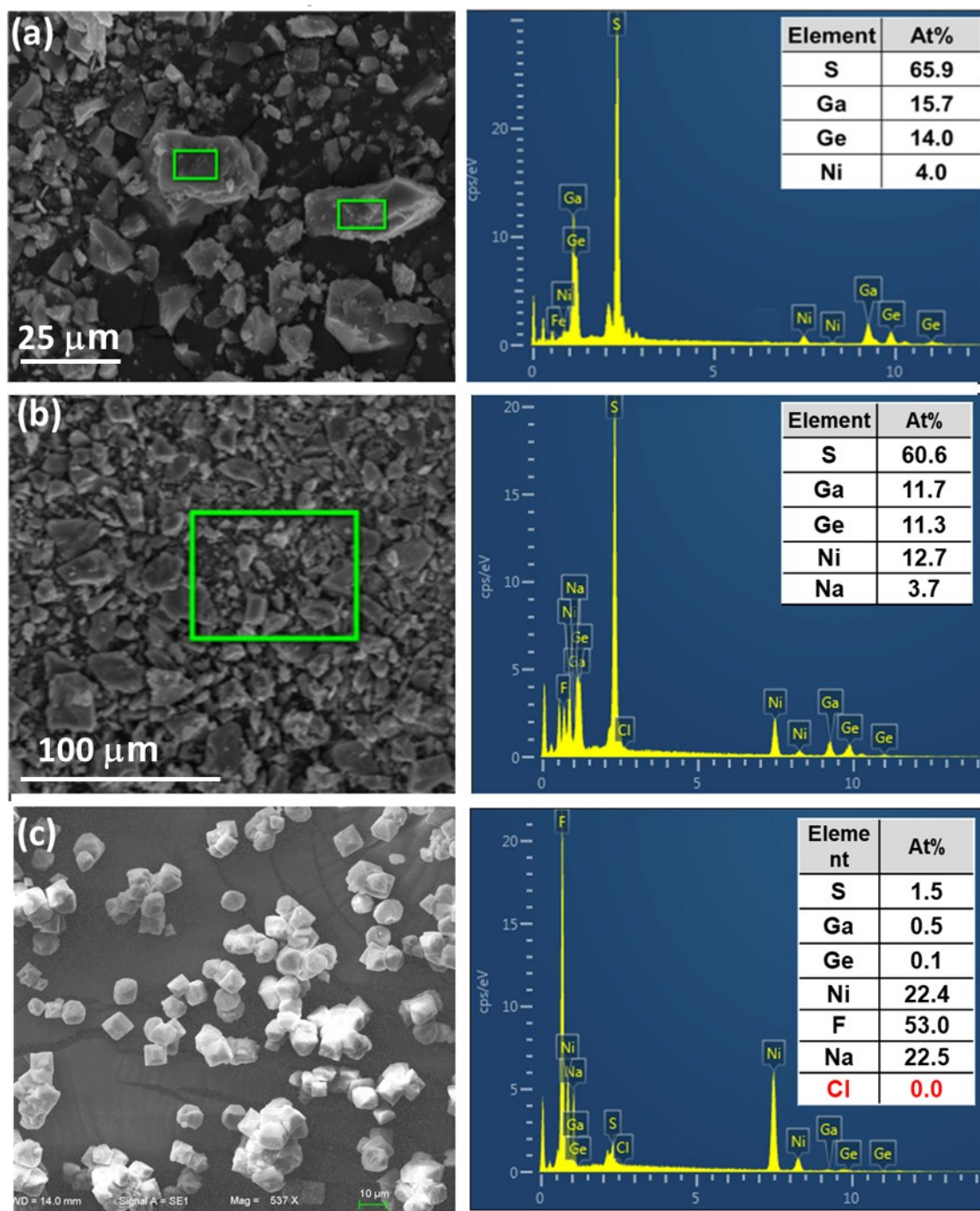
Fig. S6 SEM images and the corresponding EDX elemental analysis of Ni@CSZ, Ni(OH)$_2$ NPs@CSZ and Ni/CSZ-NaF (2 M).
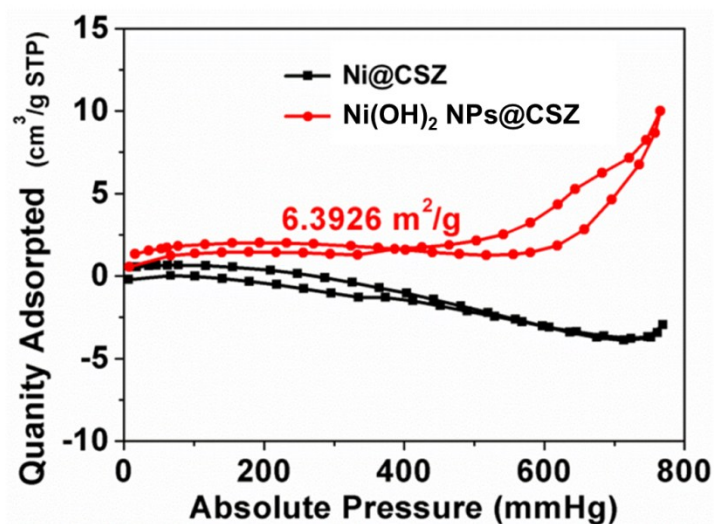
Fig. S7 N_2 adsorption-desorption isotherm measured at 77 K for Ni@CSZ and Ni(OH)$_2$ NPs@CSZ (degas 12 h at 100℃).
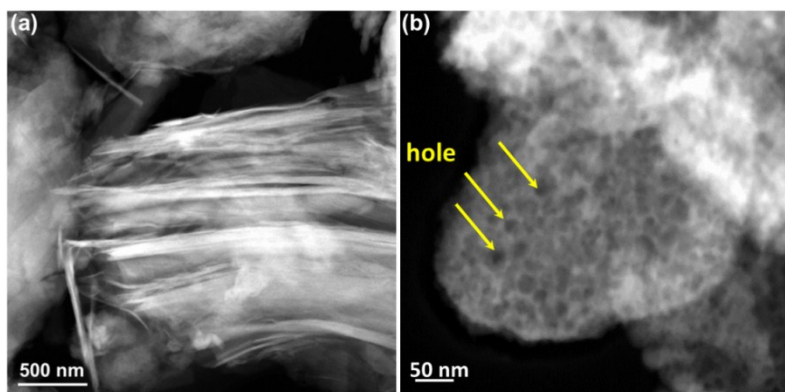
Fig. S8 High-angle annular dark field scanning transmission electron microscopy (HAADF-STEM) images of original CSZ (a) and Ni(OH)$_2$ NPs@CSZ (b).
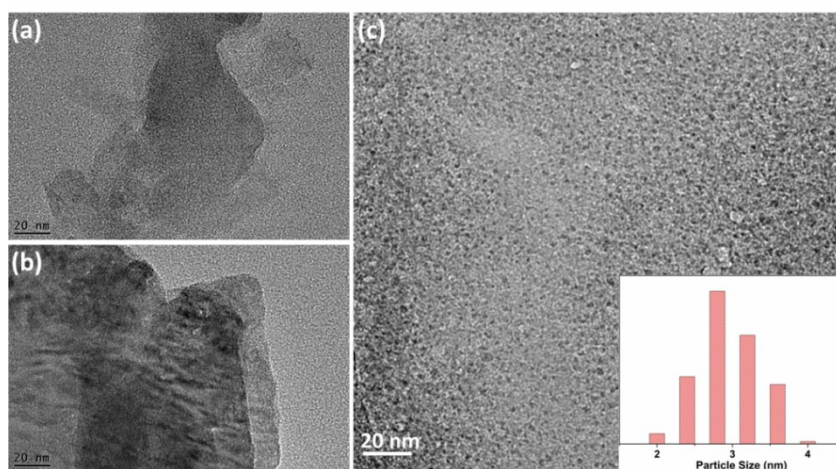
Fig. S9 HRTEM images: (a) Ni@CSZ; (b) CSZ-NaF (1 M); (c)Ni(OH)$_2$ NPs@CSZ. Inset: the distribute and size of Ni(OH)$_2$ NPs in CSZ.
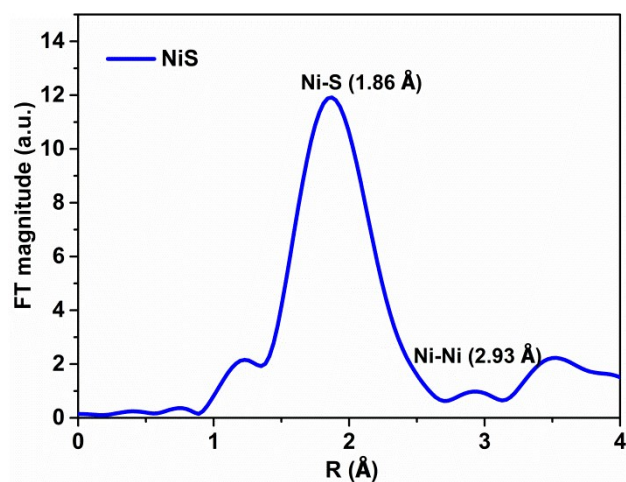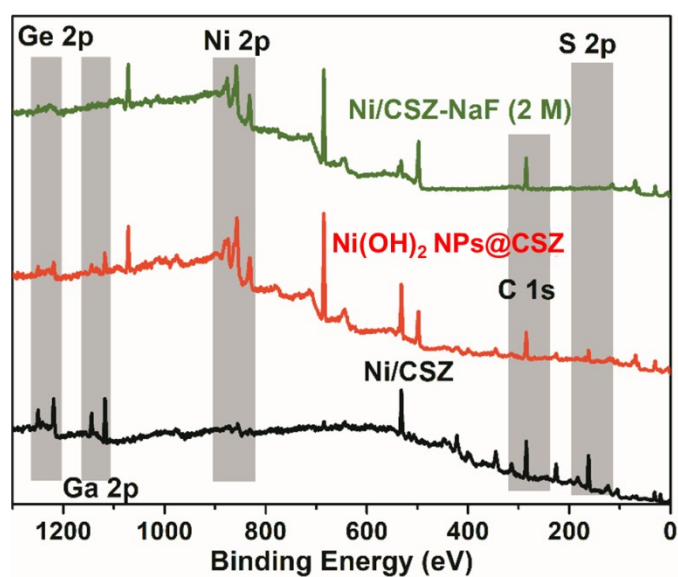
Fig. S10 Fourier transform curve of the EXAFS for NiS.

Fig. S11 XPS survey spectra of Ni@CSZ, Ni(OH)$_2$ NPs@CSZ and Ni/CSZ-NaF (2M).
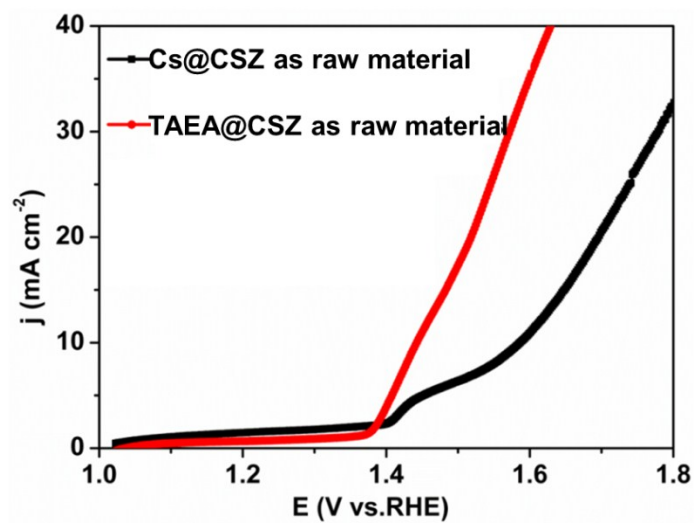

Fig. S12 LSV curves of CSZ and Cs@CSZ treated by NaF (1 M) and NiCl$_2$ (1 M) solution.
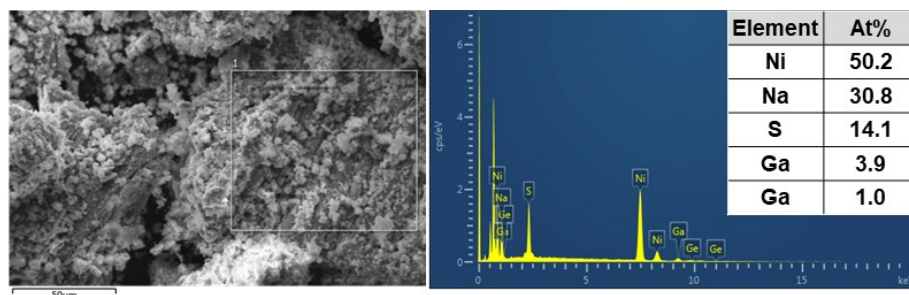
Fig. S13 SEM images and corresponding element analysis of Cs@CSZ treated by Ni^{2+} ions and NaF (1 M).
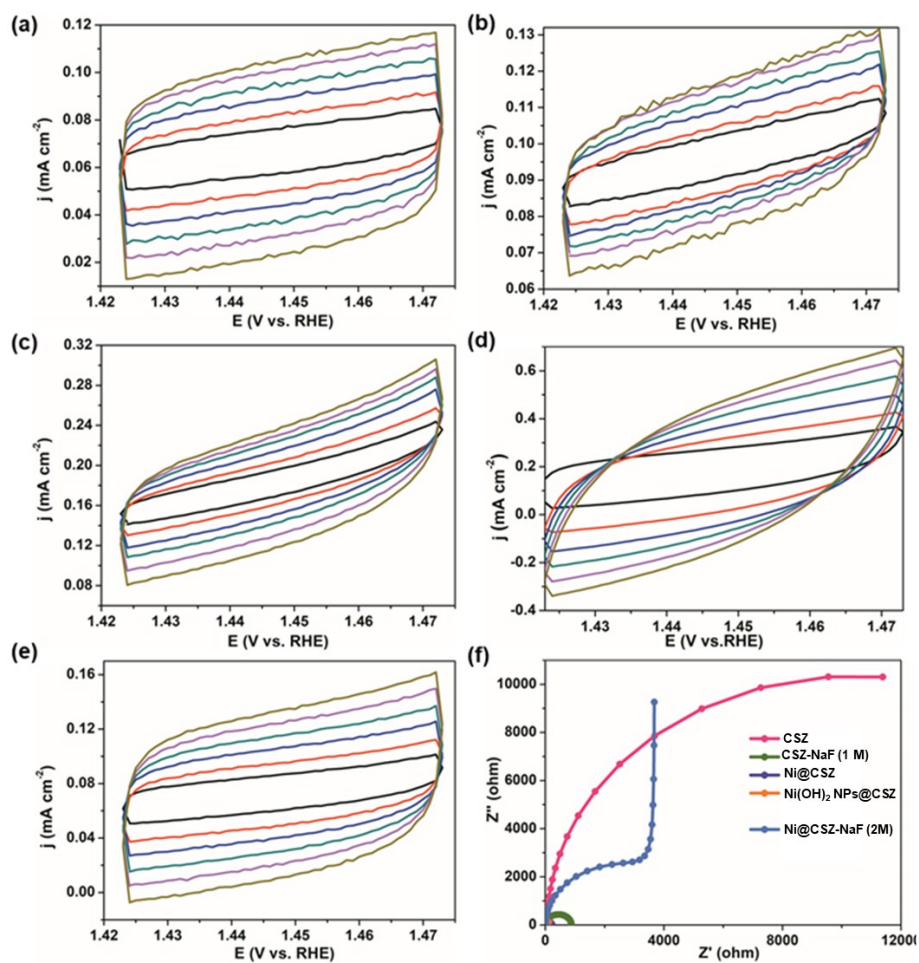

Fig. S14 (a-e) Cyclic voltammograms for double-layer capacitance measurements to estimate C_{dl} of CSZ, CSZ-NaF, Ni@CSZ, Ni(OH)$_2$ NPs@CSZ, Ni/CSZ-NaF (2 M); and (f) the corresponding electrochemical impedance spectroscopy.
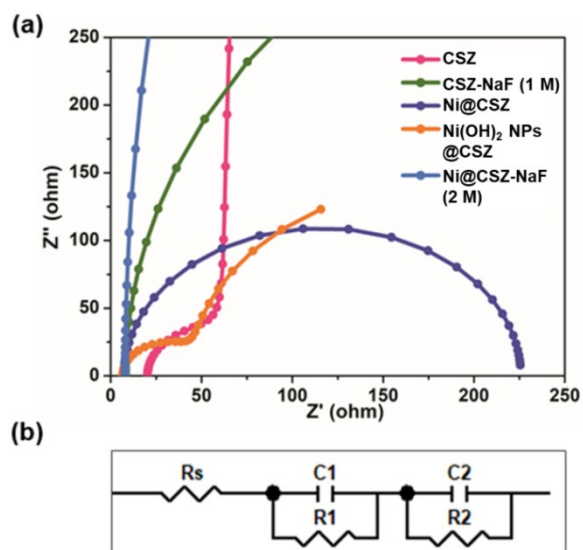
Fig. S15 (a) The electrochemical impedance spectroscopy of as-prepared materials in 1 M KOH; (b) The equivalent circuit model for electrochemical impedance tests.
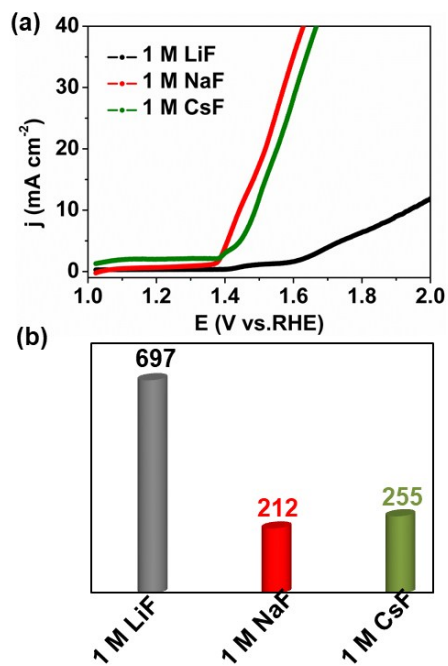

Fig. S16 The LSV curves and the comparison about over-potential of Ni(OH)$_2$ NPs@CSZ-MF (M = Li, Na, Cs) at current density at 10 mA cm^{-2}.
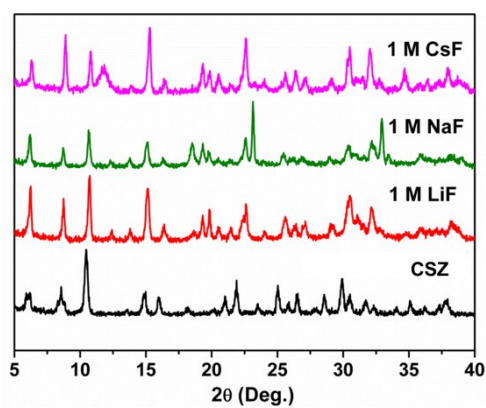
Fig. S17 Powder XRD patterns of pure CSZ and Ni(OH)$_2$ NPs@CSZ-MF (M = Li, Na, Cs).
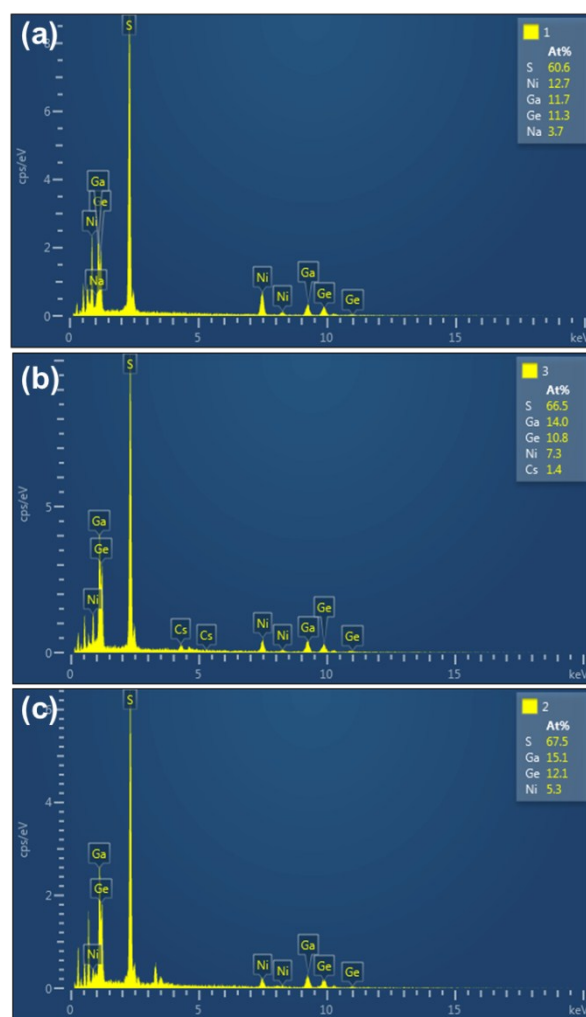

Fig. S18 The EDX element analysis: (a) Ni(OH)$_2$ NPs@CSZ-NaF (1 M); (b) Ni(OH)$_2$ NPs@CSZ-CsF (1 M); (c) Ni(OH)$_2$ NPs@CSZ-LiF (1 M).

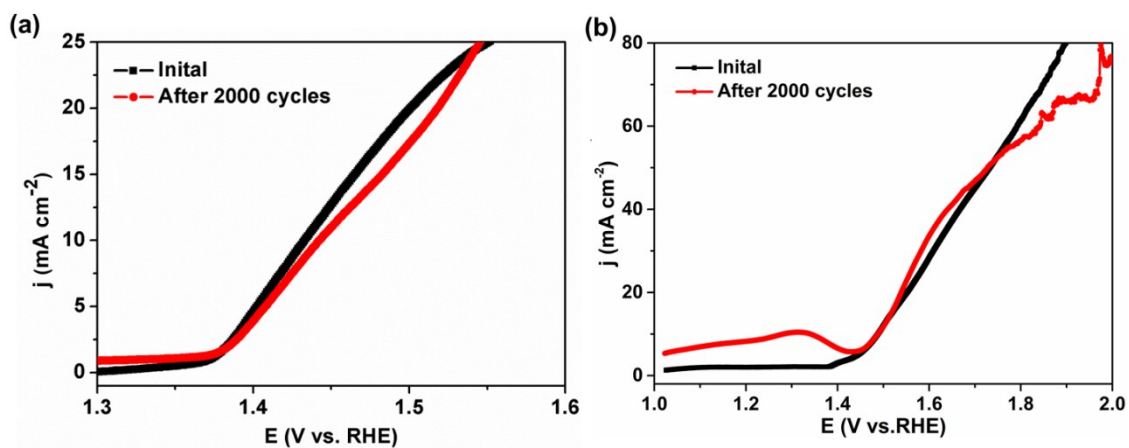**Fig. S19** LSV curves of Ni(OH)$_2$ NPs@CSZ-NaF (a) and Ni(OH)$_2$ NPs@CSZ-CsF (b) before and after 2000 cycles.
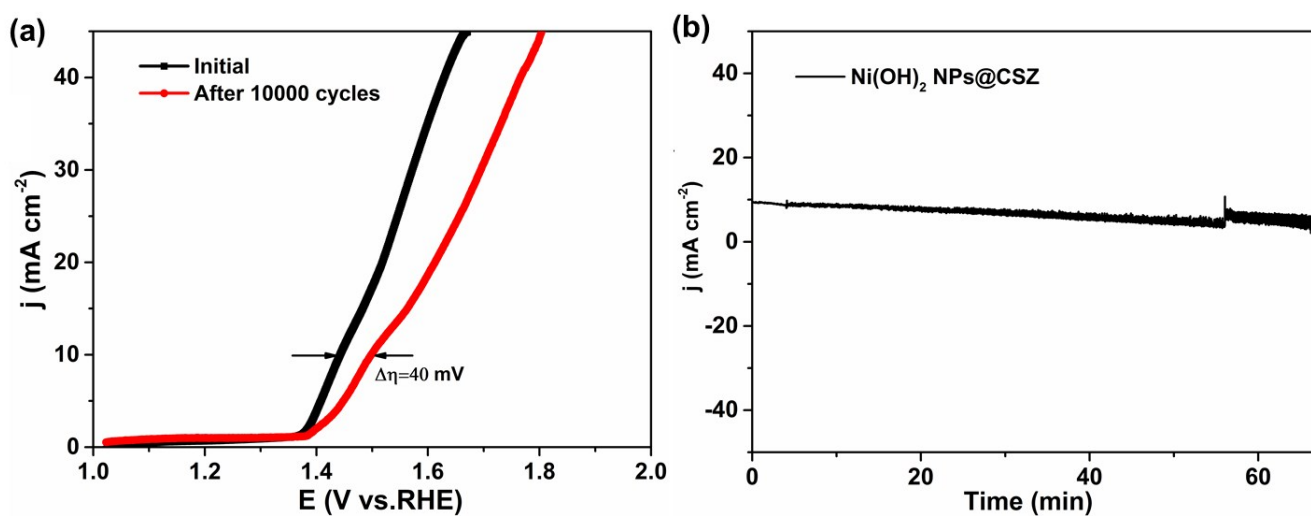
Fig. S20 (a) LSV curves of Ni(OH)$_2$ NPs@CSZ-NaF before and after 10000 cycles; (b) i-T curves of Ni(OH)$_2$ NPs@CSZ after 10000 cycles.
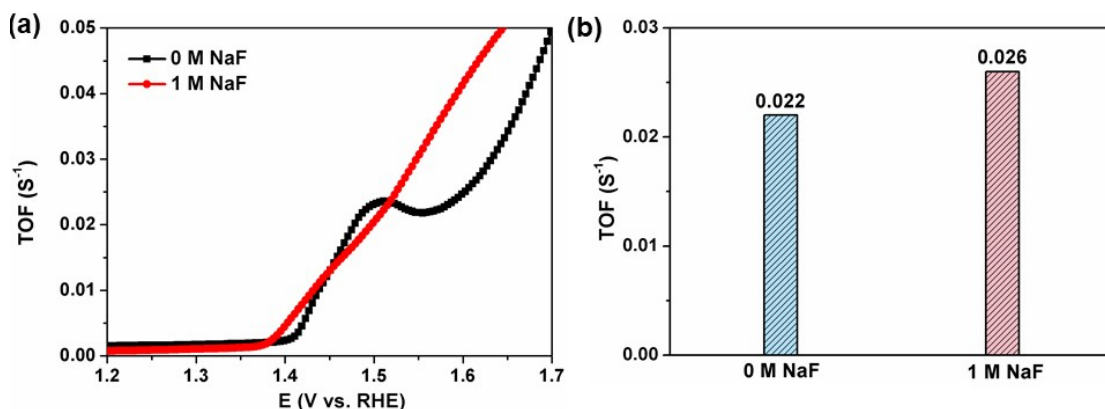
Fig. S21 (a) TOF polts with respect to the applied potential of Ni/CSZ and Ni(OH)$_2$ NPs@CSZ; (b) TOF values of Ni@CSZ at potential of 300 mV.
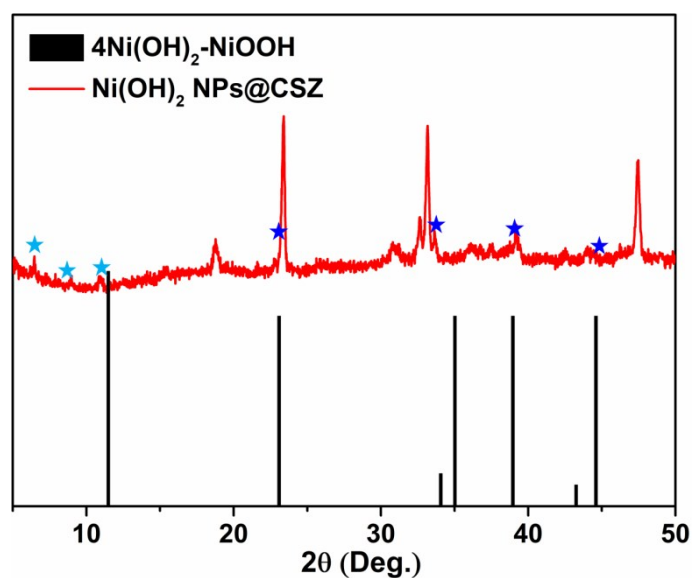
Fig. S22 PXRD pattern of Ni(OH)$_2$ NPs@CSZ after OER test.
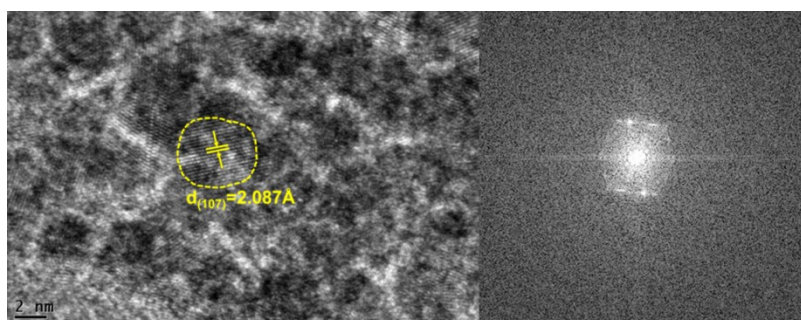
Fig. S23 The lattice fringe and corresponding selected area electron diffraction (SAED) of Ni(OH)$_2$ NPs@CSZ after OER test.
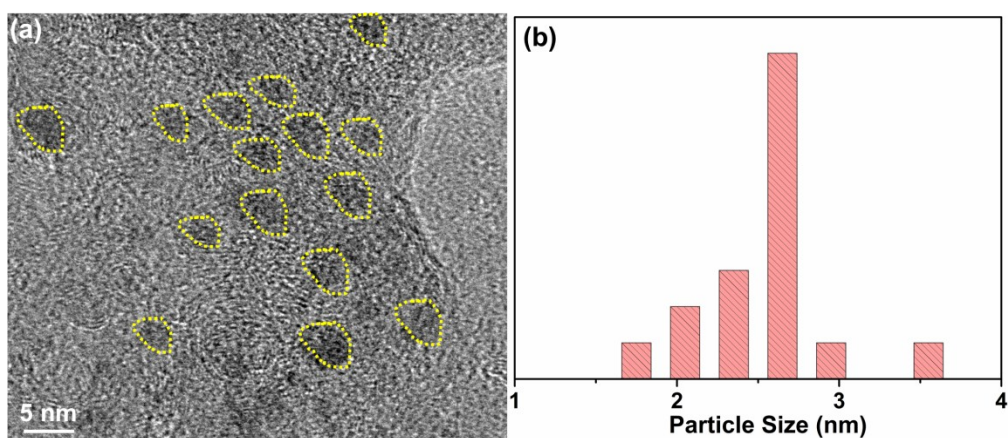
Fig. S24 The size distribution of Ni(OH)$_2$ NPs in CSZ after OER test.
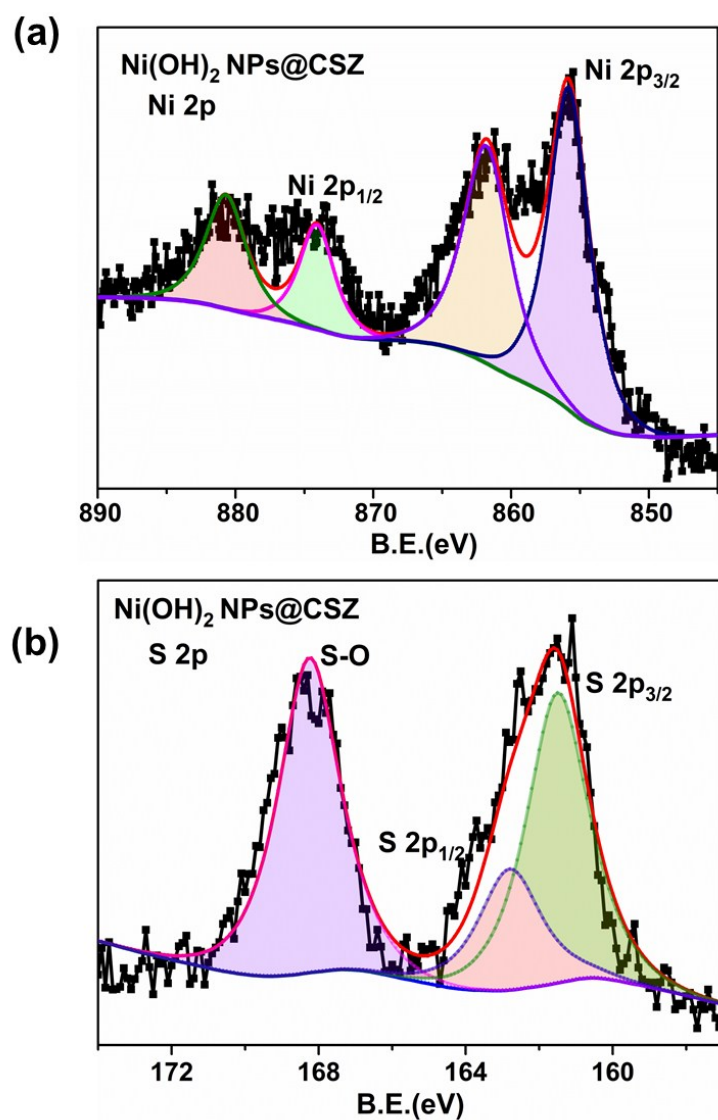
Fig. S25 XPS spectra of Ni(OH)$_2$ NPs@CSZ after OER test.
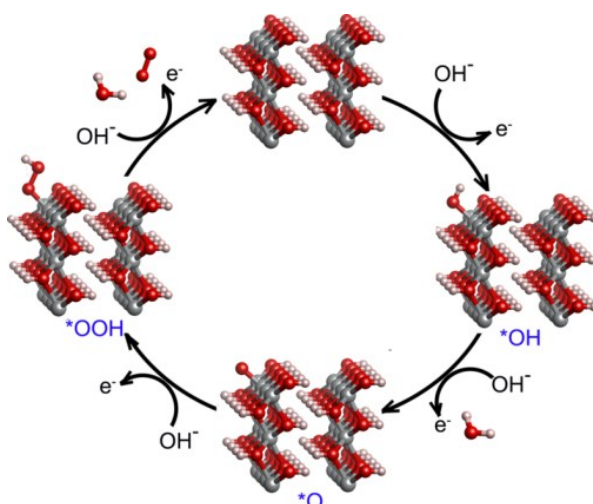
Fig. S26 The most probable OER mechanisms on β-Ni(OH)$_2$.
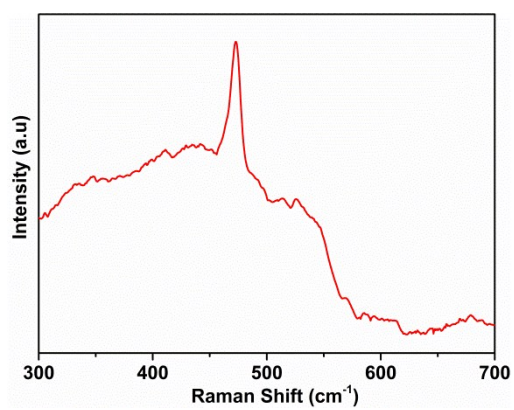
Fig. S27 The Raman spectrum of Ni(OH)$_2$ NPs@CSZ after OER test.
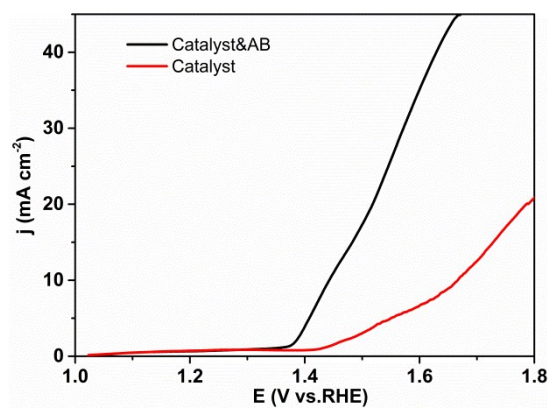
Fig. S28 The LSV curve of catalyst&AB and catalyst without AB.

Table S1 Comparison about ionic charge and ionic radius as well as electronegativity of Ga/Ge/Ni.

Element	Ionic Charge	Ionic Radius	Electronegativity [a]
Ga	3^+	0.61	1.81
Ge	4^+	0.53	2.01
Ni	2^+	0.69	1.91

[a] Pauling electronegativity scale

Table S2 Comparison of OER performance of some $Ni(OH)_2$-related catalysts reported previously.

| Catalysts	η (mV)	Substrate	Existence Form	Size	Electrolyte	Ref.
NiFe-OH-F	η_{10}=176	NF	nanosheet		1 M KOH	[2]
$Ni(OH)_2/Ni_3S_2$	η_{10}=210	NF	nnnosheet	~ 1.8 nm	1 M KOH	[3]
$Ni(OH)_2$ NPs@CSZ	**η_{10}=212**	**GCE**	**nanoparticle**	**~ 3.0 nm**	**1 M KOH**	**This work**
α-$Ni(OH)_2$	η_{10}=220	NF	nanoparticle	~ 60 nm	1 M KOH	[4]
MoS_2-$Ni(OH)_2$	η_{10}=233	NF	nanorod		1 M KOH	[5]
W-$Ni(OH)_2$	η_{10}=237	GCE	nanosheet		1 M KOH	[6]
benzoate-$Ni(OH)_2$/NF	η_{60}=242	NF	nanobelt		1 M KOH	[7]
NiFe/$Ni(OH)_2$/NiAl	η_{10}=246	NiAl alloy foil	nanosheet		KOH	[8]
N-CNTs/$Ni(OH)_2$	η_{10}=254	NF	nnnosheet		1 M KOH	[9]
$Ni(OH)_2$ NPs@CSZ-CsF (1 M)	**η_{10}=255**	**GCE**	**nanoparticle**		**1 M KOH**	**This work**
Fe(0.5)-doped β-$Ni(OH)_2$ catalyst	η_{10}=260	GCE			1 M KOH	[10]
petal-like $Ni(OH)_2$-NP	η_{10}=260	GCE	petal-like nanosheet		1 M KOH	[11]
$Ni(OH)_2/Ni_3S_2$	η_{20}=270	NF	nanosheet		1 M KOH	[12]
N-rGO-MoS_2-$Ni(OH)_2$	η_{10}=271	CC	nanoparticle		1 M KOH	[13]
$(Ni-Fe)S_x/NiFe(OH)_y$	η_{100}=290	NF	film		1 M KOH	[14]
$Ni(OH)_2$-Ag-RGO	η_{10}=292	GCE	nanosheet		1 M KOH	[15]
ultrathin $Ni(OH)_2$ nanosheet	η_{10}=295	FTO			1 M NaOH	[16]
Ni-B@$Ni(OH)_2$	η_{100}=300	NF	nnnosheet		1 M KOH	[17]
$Ni(OH)_2/\beta$-like FeOOH	η_{10}=300	FTO	nanorod		1 M KOH	[18]
β-$Ni(OH)_2$ nanosheets decorated with β-$Ni(OH)_2$ nanoburls	η_{10}=300~303	GCE	nanosheet and nanoburl		1 M KOH	[19]
$Ni(OH)_2$/NF	η_{50}=330	NF	nanosheet		1 M KOH	[20]
α-$Ni(OH)_2$	η_{10}=331	GCE	nanocrystal	~86 nm	0.1 M KOH	[21]
B-$Ni(OH)_2$	η_{10}=340	GCE	nanosheet		0.1 M KOH	[22]
$Ni(OH)_2$-TCNQ	η_{100}=354	CF	nanoparticle	~6.1 nm	1 M KOH	[23]
Au-$Ni(OH)_2$-NC	η_{10}=355	GCE	nanoporous		0.1 M KOH	[24]
α-$Ni(OH)_2 \cdot 0.75H_2O$	η_{100}=357	NF	nanofilm		1 M KOH	[25]

Note: GCE: glassy carbon electrode; CF:copper foam; NF: nickel foam; CC:carbon cloth

Table S3 DFT-calculated values of energy and ΔG_{abs} about β-Ni(OH)$_2$.

Compound	Energy (eV)	ΔG_{abs}	Value
Surface	-193.53039084	$\Delta G1$	0.406040845
Surface+OH	-204.03267302	$\Delta G2$	2.345709145
Surface+O	-198.27268705	$\Delta G3$	1.123331775
Surface+OOH	-208.05767830	$\Delta G4$	1.044918235

Table S4 The free energies of the intermediates on β-Ni(OH)$_2$ at different potential U values.

	U=0 V	U=1.23 V	U=2.35 V
G0	0.0000000000	0.000000000	0.0000000
G1	0.4060408450	-0.823959155	-1.9439592
G2	2.7517499900	0.291749990	-1.9482500
G3	3.8750817650	0.185081765	-3.1749182
G4	4.9200000000	0.000000000	-4.4800000

Table S5 DFT-calculated values of energy and ΔG_{abs} about S-doped β-Ni(OH)$_2$.

Compound	Energy (eV)	ΔG_{abs}	Value
Surface	-188.76827059	$\Delta G1$	0.899640755
Surface+OH	-198.77695286	$\Delta G2$	2.106399435
Surface+O	-193.25627660	$\Delta G3$	1.381501975
Surface+OOH	-202.78309765	$\Delta G4$	0.532457835

Table S6 The free energies of the intermediates on S-doped β-Ni(OH)$_2$ at different potential U values.

	U=0 V	U=1.23 V	U=2.35 V
G0	0.00000000	0.00000000	0.00000000
G1	0.89964075	-0.33035925	-1.20735925
G2	3.00604019	0.54604019	-1.20795981
G3	4.38754216	0.69754216	-1.93345784
G4	4.92000000	0.00000000	-3.50800000

Reference

1 X. Bu, N. Zheng, B. Wang, P. Feng, *Science*, 2002, **298**, 2366-2369.

2 B. Zhang, K. Jiang, H. Wang, S. Hu, *Nano Lett.*, 2019, **19**, 530-537.

3 Q. Xu, H. Jiang, H. Zhang, Y. Hu, C. Li, *Appl. Catal. B: Environ.*, 2019, **242**, 60-66.

4 A. Balram, H. Zhang, S. Santhanagopalan, *Mater. Chem. Front.*, 2017, **1**, 2376-2383.

5 C. Wei, C. Liu, L. Gao, Y. Sun, Q. Liu, X. Zhang, J. Guo, *J. Alloys Compd.*, 2019, **796**, 86-92.

6 J. Yan, L. Kong, Y. Ji, J. White, Y. Li, J. Zhang, P. An, S. Liu, S.T. Lee, T. Ma, *Nat. Commun.*, 2019, **10**, 2149-2159.

7 M. Ma, R. Ge, X. Ji, X. Ren, Z. Liu, A.M. Asiri, X. Sun, *ACS Sustainable Chem. Eng.*, 2017, **5**, 9625-9629.

8 S. Niu, W. Jiang, T. Tang, Y. Zhang, J. Li, J. Hu, *Adv. Sci.*, 2017, **4**, 1700084-1700090.

9 J. Wu, J. Subramaniam, Y. Liu, D. Geng, X. Meng, *J. Alloys Compd.*, 2018, **731**, 766-773.

10 K. Zhu, H. Liu, M. Li, X. Li, J. Wang, X. Zhu, W. Yang , *J. Mater. Chem. A*, 2015, **5**, 7753-7759.

11 C. Luan, G. Liu, Y. Liu, L. Yu, Y. Wang, Y. Xiao, H. Qiao, X. Dai, X. Zhang, *ACS Nano*, 2018, **12**, 3875-3885.

12 X. Du, Z. Yang, Y. Li, Y. Gong, M. Zhao, *J. Mater. Chem. A*, 2018, **6**, 6938-6947.

13 S. Debata, S. Banerjee, P. K. Sharma, *Electrochimi. Acta*, 2019, **303**, 257-267.

14 Q. Che, Q. Li, Y. Tan, X. Chen, X. Xu, Y. Chen, *Appl. Catal. B: Environ.,* 2019, **246**, 337-348.

15 X. Zhao, X. Ding, Y. Xia, X. Jiao, D. Chen, *ACS Appl. Nano Mater.*, 2018, **1**, 1476-1483.

16 P. Tian, Y. Yu, X. Yin, X. Wang, *Nanoscale*, 2018, **10**, 5054-5059.

17 X. Liang, R. Dong, D. Li, X. Bu, F. Li, L. Shu, R. Wei, J. Ho, *ChemCatChem*, 2018, **10**, 4555-4561.

18 K. Zhu, G. Zhu, J. Wang, Y. Zhu, Z. Zou, W. Huang, *Chem. Asian J.*, 2017, **12**, 2720-2726.

19 S. Anantharaj, P. E. Karthik, S. Kundu, *Catal. Sci. Technol.,* 2017, **7**, 882-894.

20 Y. Rao, Y. Wang, H. Ning, P. Li, M. Wu, *ACS Appl. Mater. Inter.*, 2016, **8**, 33601-33607.

21 M. Gao, W. Sheng, Z. Zhuang, Q. Fang, S. Gu, J. Jiang, Y. Yan, *J. Am. Chem. Soc.*, 2014, **136**, 7077-7084.

22 Z. Zhang, T. Zhang, J. Y. Lee, *ACS Appl. Nano Mater.*, 2018, **1**, 751-758.

23 X. Guo, R. Kong, X. Zhang, H. Du, F. Qu, *ACS Catal.*, 2017, **8**, 651-655.

24 P. Kanagavalli, R. Sudha, S. Boopathi, S. S. Kumar, *Electrochem. Commun.*, 2017, **82**, 61-65.

25 K. Yao, M. Zhai, Y. Ni, *Electrochim. Acta*, 2019, **301**, 87-96.